On the impact of porous media microstructure on rainfall infiltration of thin homogeneous green roof growth substrates

(article starts on next page)

1 # On the impact of porous media microstructure on
2 # rainfall infiltration of thin homogeneous green roof
3 # growth substrates

4 Kaj Pettersson[a,*], Dario Maggiolo[b], Srdjan Sasic[b], Pär Johansson[a], Angela
5 Sasic-Kalagasidis[a]

6 [a]*Dpt. Architecture & Civil Engineering, Chalmers University of Technology,*
7 *Chalmersplatsen 4, 412 96 Göteborg*
8 [b]*Dpt. Mechanics & Maritime Sciences, Chalmers University of Technology,*
9 *Chalmersplatsen 4, 412 96 Göteborg*

10 **Abstract**

Green roofs are considered an attractive alternative to standard storm water
management methods; however one of the primary issues hindering their pro-
liferation is the lack of data regarding their ability to retain and reduce storm
water under a variety of climatic conditions. This lack of data is partly due
to the complexity of physical processes involved, namely the heterogeneous
microscopic behavior that characterize flows in unsaturated porous media.
Such an anomalous behavior is difficult to predict a priori, especially in the
presence of layered structures. This paper examines water infiltration of a
green roof at the pore-scale with the aim to evaluate the effect of the porous
microstructure in thin substrate layers. In such layers, the thickness of the
medium and the particle size are within the same order of magnitude and the
effect of the packing arrangement on the flow dynamics can be pronounced.
In this study, three packing arrangements and two different hydraulic heads,
analogous to extreme rainfall events typical of Scandinavia, are investigated
by means of direct numerical simulations based on the lattice Boltzmann

*Corresponding author
Email address:* `kajp@chalmers.se` (Kaj Pettersson)

method. The results show that a wider variability of pore sizes in a thin medium can be linked directly to flow pathing preference and consequently less homogenized flow in the primary flow direction. This situation corresponds to intermittent flow behavior at the pore-scale level and reduced macroscopic infiltration rates. This observation unveils the possibility of designing innovative green roof growth substrates: by tuning the particle size and thickness of the layers composing the medium the desired green roof detention time can be attained.

---

1. Introduction

14   Climatic predictions in northern latitudes indicate a long-term overall in-

15 crease in rainfall intensity and frequency, leading to increased flooding risks

16 in urban environments [1]. This trend and its effects such as urban flooding

17 have already been recorded in Scandinavia as well as felt across Europe and

18 beyond. Due to the cost and difficulty associated with modification of exist-

19 ing storm water management networks it is necessary to examine alternative

20 methods by which excess storm water can be detained and removed. One

21 such candidate is the use of green and blue roofing in urban environments,

22 capable of efficient infiltration, detention and drainage of storm water. Green

23 roofs are defined as any roofing structure that incorporates living vegetation

24 in a growth substrate and commonly additional layers for drainage, a root

25 barrier and waterproofing. Blue roofs are specifically intended for storm wa-

26 ter management and may incorporate several of the layers mentioned above,

2

however they may not be vegetated. The use of green roofs reduces additional spatial planning in urban environments for storm water drainage and catchment that would otherwise be necessary. By using the rooftops it is possible to achieve greater vegetated areas in cities without significant disruption to the systems and structures already in place.

There already exists significant interest in the use of green and blue roofs internationally for a variety of reasons. These reasons range from urban pollution and noise reduction [2] to urban heat island reduction [3]. With the inclusion of their use for urban storm water management it is understandable that interest for the installation of such roofs is increasing, though there remain a few hindrances to the development and implementation of such installations. The primary factor impeding the growth in interest and use of green and blue roofs lies in the lack of sufficient available quantified data. The data of primary interest consists of peak runoff delay time and quantity reduction, total retention capacity, time required for evaporative drying of the soil, and thermal properties. This type of information is difficult to obtain as it is highly dependent upon prior water saturation levels in the soil, soil material composition and compaction, plant type, and temperature to name the largest factors. If we consider only storm water detention, this performance data is relevant not only to city planners and the producers themselves but also to the building designers who must take into account the structural implications of fully saturated roofs. The secondary issue is the higher price of such constructions and regular maintenance schedules required to keep the roofs in good health.

These issues can be addressed by the determination of storm water in-

filtration, detention and drainage through these constructions. Storm water detention encompasses the delay and peak flow reduction of runoff throughout and after a rainfall event by the mechanical process of liquid infiltration of the soil. Alternatively, retention covers the reduction of runoff by the processes of capturing infiltrating water in the pore structure and its subsequent removal by way of evaporation and transpiration, including the contribution of vegetation. Previous research on this topic is primarily experimental and covers laboratory scale experiments through full-scale green roofs. A heavily important factor in the performance of green roofs is evapotranspiration as outlined in [4, 5] due to the nature of liquid storage in porous soil substrates. While this physical phenomenon cannot be ignored when discussing the long-term performance of green roofs, the time scale over which it operates makes it of little use in short-term extreme rainfall events, which are of primary importance. Studies by Hamouz et al. [6] and Stovin et al. [7] have found that while green roofs perform well on isolated rainfall events with regard to retention and detention of storm water they are less effective over several events in close temporal proximity, particularly if one or more events are of a greater intensity. Of particular note is that retention of storm water is severely reduced by prior rainfall events and the best one can generally hope for is simply a detention within the system.

Other experimental work on green roofs has focused on the plant ecology [8, 9] with the aim of greater climatic resilience and possible additional benefits to storm water performance in terms of evapotranspirative efficiency. A final aspect of experimental research is the determination of the growth substrate material composition on detention and retention performance. Work

by Stovin et al. [9] has shown that different mixes of substrate materials has a measurable impact on the performance, suggesting substrate composition can be modified to improve performance. A further point of note of these studies is the state of the growth medium with regard to prior wetting and current liquid presence on the imbibition and drainage of subsequent storm water.

Beyond the use of more commonplace hydrological models such as HY-DRUS, SWMM and similar efforts [10, 11] there has been little work on the application of more detailed numerical modeling to accurately predict storm water flow in green roofs. The modeling techniques of best notoriety are traditional computational fluid dynamics (CFD) using finite volume and finite element methods. These modeling methods are ideal for use in the prediction of infiltration and drainage dynamics as well as in aiding the roof design and optimization for a variety of climatic conditions. The largest drawback of such models lies in accurately capturing the hysteresis observed in liquid infiltration of porous media such as soil. The hysteresis is caused by the interdependency of the liquid and gas phase flows on each other as well as the pore network morphology of the solid matrix; and accurately modeling this relationship remains an unresolved problem in the discipline [12].

The difficulty of characterizing the interaction between a liquid and a gas within a pore network has led to the widespread use of the lattice Boltzmann method (LBM) for this problem. The method is advantageous for use on problems such as this due to a variety of reasons. The method solves the Boltzmann equation of particle motion at the mesoscopic scale and therefore allows for efficient computation as well as ease of boundary condition defini-

tion in complex geometries. Another advantage is the ability of the method to provide excellent result resolution for such problems that are not easily handled by traditional CFD methods. Many researchers have focused their efforts on determining the interactions and relevant parameters responsible for the hysteresis and details can be found in [13, 14, 15]. These works attempted to construct unique functions relating a combination capillary pressure, saturation and liquid-gas interfacial area. Others have applied integral geometry to define pore structure influence on capillary flow in terms of an Euler characteristic [16]. What is clear is that there is a contribution from the pore morphology on the infiltration and drainage process that must be explored in more detail at the microstructural (pore) scale.

This work explores the effect of the microstructure of thin substrate layers on water infiltration dynamics at the pore scale by using LBM on 3 domains with dissimilar properties. The microstructure for each domain is modified through alteration of the particle diameter in a homogeneous packed bed analogous to a representative thin soil volume. We define a medium "thin" when the thickness of the medium and the particle size are within the same order of magnitude. The infiltration is driven by hydraulic pressure applied via standing surface water whose height is determined by rainfall data taken from Gothenburg, Sweden. The results indicate the microstructure can positively and negatively impact the infiltration of water into a thin porous medium. This behavior can be explained by the concept of capillary barriers [17] determined by the energy balance in the pore network [18]. When the particle sizes are increased in relation to the thickness of the porous medium we see a decrease in flow homogeneity. When the porous medium is insuf-

6

ficiently thick the particle packing encourages inhomogeneous flow profiles, and consequently gives rise phenomenon such as the capillary barrier in some pore networks that alters the global rate of water infiltration. This observation suggests the possibility of controlling the green roof detention time in green roofs by adopting an optimized layered structure in their design.

In section 2 the methodology for the geometry construction and numerical simulations is detailed. Section 3 includes the results and accompanying discussion and a conclusion is given in section 4.

2. Materials and methods

2.1. Lattice Boltzmann method

The Lattice Boltzmann method solves the Boltzmann transport equation which consists of a phase space discretized into a lattice mesh and is selected for this work for several reasons. These reasons stem from the fact that the method operates on the micro and mesoscale and therefore inherits the advantages from molecular dynamics and kinematic theory. These advantages include efficient parallelization in computation and ease of handling complex geometries due to the simplified nature of the boundary condition requirements. More importantly, the method provides the ability to answer fundamental questions regarding a given flow at great resolution. Each individual lattice structure consists of a centroid and nodes on the convex shell of the lattice geometry. Fictive particles travel between the nodes governed by a probability assigned for travelling to each position on the lattice. The probabilities are chosen based upon the lattice geometry and facilitate the recovery of the macroscopic properties of the fluid. This allows for complex boundaries to be defined with simplicity using bounce-back condition on the boundaries, negating the need for mesh refinement at the boundaries as required in traditional CFD modeling. The second reason for the application of this method lies in its innate ease for parallelization with regard to computation. Since the lattice mesh is defined in a grid pattern by definition the computations can be distributed without loss of information, thus drastically increasing the computational speed [19].

In this work a 3-dimensional regular cubic lattice with 18 nodes on the

convex shell and a centroid, written as D3Q19, is used. The lattice Boltz-
mann code has been previously used for several different applications. For
a validation of the two-phase lattice Boltzmann algorithm, the reader is re-
ferred to [20]. The solved equation is given as

$$f_r(\boldsymbol{x} + \boldsymbol{c}_r \delta t, t + \delta t) - f_r(\boldsymbol{x}, t) = -\tau^{-1}(f_r(\boldsymbol{x}, t) - f_r^{eq}(\boldsymbol{x}, t)) + F_r \qquad (1)$$

where $f_r(\boldsymbol{x}, t)$ is the distribution function at position $\boldsymbol{x}$ and time t along
the r-th direction; $\boldsymbol{c}_r$ is the so-called discrete velocity vector along the r-th
direction over time interval δt; τ is the mean collision time and is related to
kinematic viscosity by $\nu = c_s^2(\tau - 0.5\delta t)$. The fluid is forced by a body force
F_r which mimics the effect of gravity. Such a force is defined following the
approach defined by Guo et al. [21],

$$F_r = \left(1 - \frac{1}{2\tau}\right) w_r \left(\frac{\boldsymbol{c}_r - \boldsymbol{u}}{c_s^2} + \frac{\boldsymbol{c}_r \cdot \boldsymbol{u}}{c_s^4} \boldsymbol{c}_r\right) (\rho \boldsymbol{g}) \qquad (2)$$

with $\boldsymbol{g}$ representing gravitational acceleration and $\boldsymbol{u}$ the fluid velocity. The
equilibrium distribution function $f_r^{eq}(\boldsymbol{x}, t)$ takes the form

$$f_r^{eq} = w_r \rho \left(1 - \frac{\boldsymbol{u}_{eq} \cdot \boldsymbol{u}_{eq}}{2c_s^2}\right), \ r = 1 \qquad (3)$$

$$f_r^{eq} = w_r \rho \left(1 + \frac{\boldsymbol{c}_r \cdot \boldsymbol{u}_{eq}}{c_s^2} + \frac{(\boldsymbol{c}_r \cdot \boldsymbol{u}_{eq})^2}{2c_s^4} - \frac{\boldsymbol{u}_{eq} \cdot \boldsymbol{u}_{eq}}{2c_s^2}\right), \ r = 2 - 19 \qquad (4)$$

where w_r is the appropriate weighting parameter for the D3Q19 lattice; ρ
is the density; c_s is the speed of sound; and $\boldsymbol{u}_{eq}$ is the velocity used for
defining the equilibrium distribution functions, which can differ from the fluid

9

hydrodynamic velocity, on the basis of the specific forcing scheme used. In the present work, we apply the Guo forcing formulation for implementing the gravitational force whereas we make use of the Shan-Chen force for simulating surface tension [22]. The macroscopic flow quantities density and velocity, $(\rho, \boldsymbol{u})$ are thus related to the hydrodynamic moments as the following:

$$\rho = \sum_r f_r \tag{5}$$

$$\rho\boldsymbol{u} = \sum_r \boldsymbol{c}_r f_r + 1/2 \ \rho\boldsymbol{g} + 1/2 \ F_{sc} \ , \tag{6}$$

and the equilibrium velocity is formulated as: [23]

$$\boldsymbol{u}_{eq} = \rho\boldsymbol{u} + (\tau - 1/2)F_{sc} \tag{7}$$

where F_{sc} is the Shan-Chen gas-liquid interaction force. A detailed discussion of the forcing schemes proposed by Shan-Chen and Guo can be found in Huang et al. [24]. The Shan-Chen model was developed to overcome the limitations of LBM in dealing with components of differing molecular mass as well as thermodynamic phase transitions [22]. It is an ideal choice since we are interested in the interaction of two immiscible fluids as well as the interaction of the microstructure with the fluids. Its fundamental feature is the addition of an inter-particle potential which adds attractive or repulsive properties in combination with the elastic collision force already present in previous models. The inter-particle force gives rise in the system to a non-ideal equation of state:

$$p = \rho c_s^2 + \frac{G}{2}c_s^2\Psi^2, \tag{8}$$

10

where liquid and gas phases coexist at the thermodynamic equilibrium state. The Shan-Chen force is given by:

$$F_{sc} = -G\Psi(\mathbf{x}, t) \sum_r w_r \Psi(\boldsymbol{x} + \boldsymbol{c}_r \delta t, t) \boldsymbol{c}_r \tag{9}$$

where G, valued -5.5 in this work, is the interaction strength between the phases and $\Psi(\rho)$ is a density-dependent pseudo potential function. Negative values of G define an attractive force and positive values a repulsive force. The pseudo-potential function calculates effective mass locally:

$$\Psi(\rho) = 1 - e^{-\rho}. \tag{10}$$

The effective mass approaches ρ itself when its value is low and obtains a saturation value when it is increased. It is capable of capturing the two important characteristics of a non-ideal flow, namely the equation of state in Eq.(8) and surface tension.

The fluid-solid interaction is determined by a moving gas-liquid contact line. This contact line is characterised by a contact angle that is chosen under equilibrium conditions, without external forces, as determined by the Young's equation. The equilibrium contact angle is implemented through spatial averaging of the density-dependent potential function. The force at the solid wall (Ψ_{wall}) is calculated using the method proposed by De Maio et al. [25] and is of the form:

$$\Psi_{wall} = N^{-1} \sum_N \Psi + \Delta_w \tag{11}$$

11

²⁰⁸ where Ψ is the density-dependent function and N the nearest fluid compu-

²⁰⁹ tational nodes. This formulation enforces a fixed density gradient at the

²¹⁰ wall and by tuning the parameter representing surplus density, Δ_w, different

²¹¹ contact angles can be represented at the desired lattice resolution. More in-

²¹² formation regarding the relationship between Δ_w and the contact angle can

²¹³ be found in Benzi et al. [26].

²¹⁴ We perform a validation of two-phase Poiseuille flow between parallel

²¹⁵ plates using the methodology described in detail by Yang and Boek [27].

²¹⁶ The results are compared to the analytical solution in Reza and Martin [28]

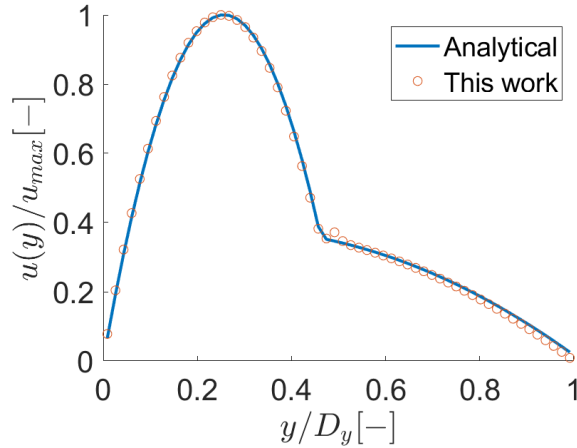in Figure 1 and the agreement is found to be very high.

Figure 1: Comparison of the numerical framework used in this work against analytical solution by Reza and Martin [28], D_y is channel width. On the y axis the two-phase velocity normalized with the maximum velocity is shown.

²¹⁷

²¹⁸ *2.2. Simulation setup*

²¹⁹ *2.2.1. Domain specifications*

²²⁰ The simulation domains are split into 2 sections; i) the surface liquid and

²²¹ ii) the porous medium consisting of a packed bed of homogeneous spher-

ical particles. The surface liquid section is a void and allows for the initialization of the wetting liquid without disruption to the porous medium below. A packed bed with uniform particle size (monodisperse) is chosen as an analogue to soil for this study so as to remove influence of particle inhomogeneities. These inhomogeneities include shape, orientation, surface roughness and hydrophilicity. These factors are neglected for this study in order to remove as much uncertainty as possible when analyzing the effect of particle packing on infiltration however in reality they contribute to the infiltration dynamics to a variable degree.

Three distinct packed beds of randomly packed homogeneous spherical particles of varying particle diameter are used for this study. A reference particle diameter was selected based upon a desired porosity and pore size reflecting the properties of lightweight expanded clay aggregate (LECA) [29]. This reference particle diameter d was converted from the given pore radius r_{eff} by applying the Revil, Glover, Pezard and Zamora (RGPZ) model [30, 31] which states

$$d = 2\Theta r_{eff}, \tag{12}$$

$$\Theta = \sqrt{\frac{ew^2}{8\epsilon_{ex}^{2w}}}, \tag{13}$$

where e is a model parameter valued $8/3$, w is the cementation exponent valued 1.5 for spherical particles and ϵ_{ex} is the experimentally determined porosity. The reference particle diameter is slightly varied to generate the other two particle diameters as listed in Table 1.

The height of the packed bed H is determined by the representative vol-

13

ume requirement for the porous medium with particle sizes as previously defined. The particle diameter is chosen as a characteristic length as it determines the pore microstructure within the porous region. A new parameter ϕ representing the packing effect of the particles on the microstructure is given by

$$\phi = \frac{H}{d}. \tag{14}$$

This quantity will be used to define the three different cases of packing arrangements and is one of the two primary parameters in this study. The values of ϕ are listed in Table 1.

The packed bed length perpendicular to the flow direction, L, is chosen such that it adheres to restrictions regarding wall effects on the calculated flow field [32]. The boundaries perpendicular to the primary flow direction must be at least 15-20 times the particle diameter to ensure wall effects are negated.

The packed beds were generated using the software Blender, which is capable of applying basic rigid body physics to objects and tracking their motion in time. Particles of a specified diameter are dropped into a box, which is later removed in the computation stage of this work. This method for creation of packed bed domains has been outlined and validated by Boccardo et al. [33] and is an efficient tool for this purpose. A binary lattice is generated for each domain by calculating each node's distance from the particle centers and defining the node accordingly. The information for the 3 domains is given in Table 1 and an example is plotted in Figure 2. Here ϵ is the porosity calculated over the domain for each case.

14

Table 1: Packed bed domain physical properties.

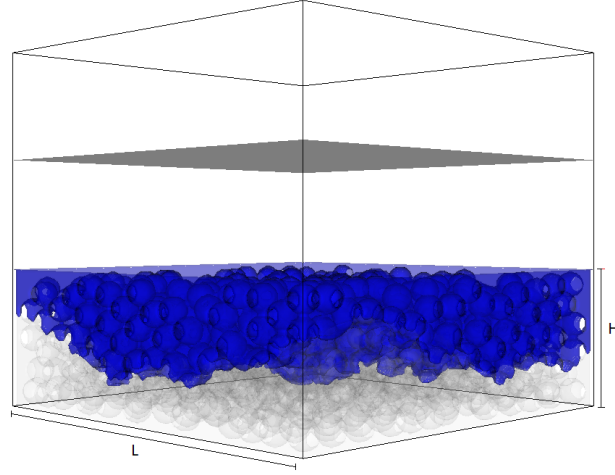| ϕ	6.7	10.1	5.1
L×L×H [mm]	15×15×5	15×15×5	15×15×5
d [mm]	0.740	0.494	0.986
ϵ	0.389	0.377	0.40

Figure 2: Domain for $\phi = 5.1$ with infiltration.

2.2.2. Boundary conditions

The boundary conditions used in all simulations in this work consist of the following: the upper and lower boundaries are periodic, the transverse boundaries are symmetric. The driving force for the flow is applied in the vertical direction. The porous medium is bordered by walls however the rest of the domain as the transverse boundaries is open.

2.2.3. Grid convergence study

To facilitate the evaluation of appropriate spatial resolution 4 grids are generated for $\phi = 6.7$ with a varying number of lattice nodes in the vertical (NH) and horizontal (NL) directions, the details of which are presented in

Table 2. A grid resolution test is undertaken using the generated grids. This

Table 2: Lattice node quantities for several grid resolutions.

	NH	NL	Total Nodes	$\Delta Cell [mm]$	d [lattice nodes]
Grid 1	50	150	1.125×10^6	0.1000	7.4
Grid 2	60	180	1.994×10^6	0.0833	8.9
Grid 3	70	210	3.087×10^6	0.0714	10.4
Grid 4	80	240	4.608×10^6	0.0625	11.8

276

test is run using single-phase isothermal air flow driven by gravity. The

determination of grid resolution accuracy is accomplished by evaluating the

relative error of the dimensionless permeability

$$K^* = K/d^2 = \frac{\overline{U}_z \mu_g}{(\rho_g g) d^2}, \tag{15}$$

where K is the permeability, $\overline{U}_z$ is the mean vertical velocity, μ_g is the gas

dynamic viscosity, ρ_g is the gas density, and g is gravitational acceleration.

The permeability is evaluated only on the inner 2/3 of the geometry in the

lateral direction to eliminate the contribution of the side wall effect as noted

by Galindo-Torres et al. [32]. It should be here noted that all the quantities

computed in this study are referred to this reduced volume in order to ensure

that the side walls does not affect the results. The two-phase flow dynamics

in porous media is determined by the balance of gravitational and capillary

forces. Therefore, the dimensionless permeability in the grid resolution test

is computed at a fixed characteristic gas capillary number $Ca_g = \rho_g g d^2 / \gamma$,

where γ is the surface tension used in the multiphase simulations. Table 3

presents the analysis of the grid resolution study and Grid 3 is chosen for all

subsequent simulations as an acceptable compromise between the relative dif-

ference of refinement and computational requirement. The relative difference of dimensionless permeability is calculated over successive grid refinements as:

$$\% \text{ Difference} = \frac{\text{Permeability}_{\text{Grid i+1}} - \text{Permeability}_{\text{Grid i}}}{\text{Permeability}_{\text{Grid i}}}. \quad (16)$$

Table 3: Grid resolution test case input and results.

Case	g [lattice units]	Re [-]	Permeability [-]	% Difference
Grid 1	6.53E-5	0.00514	0.00539	-
Grid 2	4.53E-5	0.00575	0.00500	7
Grid 3	3.30E-5	0.00634	0.00474	5
Grid 4	2.55E-5	0.00703	0.00466	2

The pore size analysis for the domains considered in this work shows the mean pore sizes range 0.25-0.35 mm which corresponds to approximately 4-6 lattice units with the resolution defined by Grid 3 (see Figure 4). This is considered a reasonable value for resolving pore scale transport, as for instance discussed by Succi [19]. Such an observation corroborates the findings of the present grid analysis and the choice of the resolution addressed as Grid 3 for our multiphase simulations.

2.2.4. Multiphase input data

Standing water is initialized within the domain directly above the porous medium. The standing water height h is used as a characteristic length due to its contribution as the body force by way of hydrostatic pressure.

Using the particle diameter and standing water height as well as the choice of lattice resolution we can convert all relevant quantities. The results are

17

categorized by two primary non-dimensional parameters; ϕ which is defined previously, and the Bond number

$$\text{Bo} \;\; = \;\; \frac{(\Delta\rho g)h^2}{\gamma}, \tag{17}$$

where g is the variable representing the gravitational component of the body force, $\Delta\rho = \rho_l - \rho_g$ is the phase density difference, and γ is the interfacial surface tension.

The Bond number represents the ratio of gravitational and surface tension forces. Work by Slobozhanin et al. showed that for Bond numbers from 0 to 5 there is little difference in the capillary pressure in tightly packed spheres [34]. Moreover if the Bond number is below 0.1 the effect of gravity can be neglected entirely.

A statistical analysis of meteorological data taken from Gothenburg, Sweden and provided by Swedish Meteorological and Hydrological Institute (SMHI) is used to determine the standing water height and consequently the Bond numbers used in this study. The statistical analysis of hourly weather data taken over the period 1995.08.04 - 2018.05.01 is used to determine the average rainfall intensity with the result being 2.5 mm/hr when rainless periods are discarded. This value is taken as the equivalent standing water height when the Bond number is 1. Since we are interested in rainfall events causing flooding this number is increased two and threefold for our simulations, analogous to a scenario where extreme rainfall occurs over a short period of time and surface water is present. This corresponds to Bond numbers of 3.96 for a standing water height of $h = 5.0$ mm and 8.92 when $h = 7.5$ mm.

In Table 4 the physical and lattice unit values for all input parameters required for the simulations are listed. Table 5 identifies the 6 cases of the study in terms of ϕ and Bo.

An additional parameter is required for implementing the multiphase simulations; the contact angle. Measurements by Ramírez-Flores et al. [35], Schrader and Yariv [36], and Fér et al. [37] demonstrate the variability of the contact angles with regard to soil aggregates and clay minerals. We motivate our choice of 82° by noting that this value lies within the range of values reported in experimental work. As reported in Fér et al. clay-coated materials exhibit a contact angle around 80° and the value decreases over time. While a singular equilibrium value is set, a dynamic contact angle arises from the simulation due to the presence of external forcing from gravity. A more complicated modeling of the contact angle is neglected on the grounds that we do not expect significant variations in the contact angle due to the low flow velocity of the system [38].

Table 4: Physical and non-dimensional input parameters. The physical time is computed via the equivalence between physical and lattice units, i.e. $t = t_{LB} \, (L^2/L_{LB}^2) \, (\nu_{LB}/\nu_l)$.

Parameter	Variable	Value	Physical value	Physical unit
Porous medium height	H	70	5.0	[mm]
Standing water height	h	70, 105	5.0, 7.5	[mm]
Particle diameter	d	10.4, 6.9, 13.8	0.74, 0.494, 0.986	[mm]
Horizontal domain length	L	210	15	[mm]
Liquid dynamic viscosity	μ_l	2.4/6	1.00e-3	[Ns/m^2]
Gas dynamic viscosity	μ_g	0.12/6	1.68e-7	[Ns/m^2]
Liquid kinematic viscosity	ν_l	1/6	1.00e-6	[m^2/s]
Gas kinematic viscosity	ν_g	1/6	1.27e-5	[m^2/s]
Liquid density	ρ_l	2.4	998	[kg/m^3]
Gas density	ρ_g	0.12	1.20	[kg/m^3]
Surface tension	γ	0.093	0.073	[N/m]
Gravity	g	3.3e-5	9.8	[m/s^2]
Time	t	1	8.5×10^{-4}	[s]

Table 5: Case specifications.

	Case 1	Case 2	Case 3	Case 4	Case 5	Case 6
ϕ	6.7	10.1	5.1	6.7	10.1	5.1
Bo	8.92	8.92	8.92	3.96	3.96	3.96

3. Results and discussion

In Figure 3, saturation Sat is plotted as a function of dimensionless time for Bo $= 8.92, 3.96$. The dimensionless time is defined as

$$t^* = \frac{t}{\sqrt{\frac{h}{g}}}. \tag{18}$$

The saturation Sat is calculated by summing the liquid nodes in the porous medium and dividing by the total void node quantity. In the Shan-Chen method, the liquid-gas spatial transition is represented with a smooth diffusive interface. A computational node belongs to the liquid node when its

20

density overcome a specific threshold. This threshold is taken in our simulations as $\sqrt{2}$, a value that corresponds to the metastable state of the non-ideal equation of state.

In Figure 3 the infiltration for all values of ϕ displays a trend with a slope ≤ 0.5 in logarithimc scale. The slope 0.5 corresponds to the theoretical solution of Washburn's equation [39] which describes the relationship between penetration length l_p of a liquid into a fixed-radius capillary tube over time without gravitational forces. The equation relates the penetration length to a diffusive coefficient D_c and time as

$$l_p \;\; = \;\; (D_c t)^{\frac{1}{2}}. \tag{19}$$

Washburn's equation does not take into account gravity and describe the capillary rise of the liquid driven by the hydrophilicity of the material; the diffusive coefficent is a function of the pore radius and the hydrophilic contact angle. Instead, in our case, the hydrophilicity of the material can be neglected, because the contact angle is close to 90°, and gravity is the force that drives liquid penetration. In this conditions, when a liquid volume penetrates a single tubular pore under pressure or gravitational forcing, an analogous formulation to Eq. (19) can be derived, with the diffusive coefficient depending on the pore radius and the gravitational force.

When we consider the liquid penetration into a porous complex structure, the physical description is more complicated, given the intricate pore network that the liquid is forced to follow during imbibition. In some pores, slow liquid infiltration induced by the intricate topology of pores boundaries can

21

be observed. The infiltration can also be intermittent, as recently observed in experiment of two-phase flows into rock samples [40], especially at low values of porosity and Bond numbers, as the ones considered in this study. In such cases, liquid infiltration in some pores can be mathematically described by a power law similar to (19), but with a smaller exponent. Therefore, at the macroscopic scale, on average, the saturation of the porous medium follows a law as:

$$Sat(t) \quad \propto \quad (D_c t)^{\alpha(t)}. \tag{20}$$

In this formulation the diffusive coefficient is determined by the hydraulic pressure and the porous microstructure and alpha is a time-dependent exponent $\alpha(t) \leq 0.5$. The saturation curves in Figure 3 follow this mathematical description.

All the curves present a slow infiltration at short and long times while at intermediate times, they exhibit the highest infiltration rate. The differences in initial saturation are due to the particle packing at the surface which is not uniform for all cases. We see clearly in the mid-range saturation values that $\phi = 10.1$ behaves similarly to Eq. (20) with slope 0.5 indicating a flow behavior similar to a single pore penetration. When $\phi = 6.7$ the infiltration is less efficient in terms of saturation and it further decreases for $\phi = 5.1$. Furthermore, as seen in Figure 3, the decreased hydraulic pressure has an adverse effect on the infiltration. It is important to note that when saturation approaches $0.7 - 0.9$ the values almost stagnate for several of the cases. This indicates some form of infiltration reduction within

22

the porous medium that is not heavily dependent upon the flow itself but rather the porous microstructure. We will discuss in the next subsection this result by categorizing the different geometries by their microstructure. Interestingly, it can be also noted that the infiltration rate appears to decrease with time, as the liquid approaches the bottom of the medium, where the spatial distribution of solid particles is significantly affected by the bottom layer where they lean. This observation is indeed further confirmed by noting that the infiltration rate between the different cases is lower for low values of ϕ, therefore when the packing effects are more pronounced.
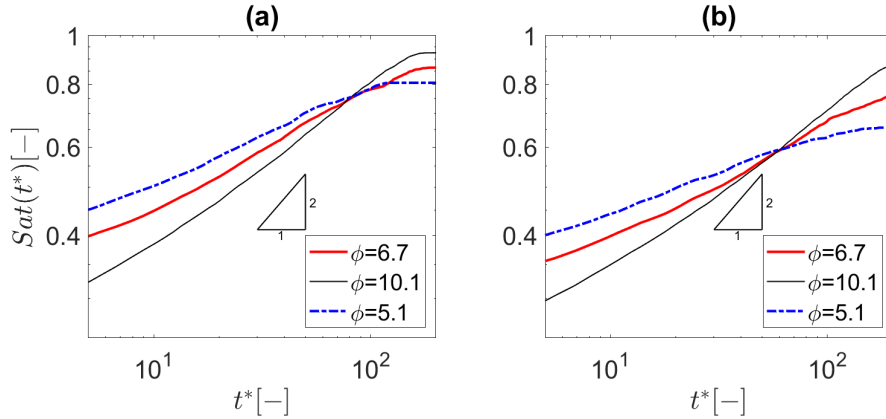
Figure 3: (a) Log-linear plot of saturation as a function of dimensionless time for $\phi = 6.7, 10.1, 5.1$ with Bo $= 8.92$. (b) Log-linear plot of saturation as a function of dimensionless time for $\phi = 6.7, 10.1, 5.1$ with Bo $= 3.96$.

3.1. Porosity as a function of porous medium depth

In Figure 4 the planar porosity orthogonal to the primary flow direction is plotted as a function of distance from the porous medium base ($H = 70$), measured in particle diameters d. At the base of the porous medium the particles are more ordered and we can see the uniformity in the packing over the first 3 particle diameters. This oscillatory effect is lost thereafter until the
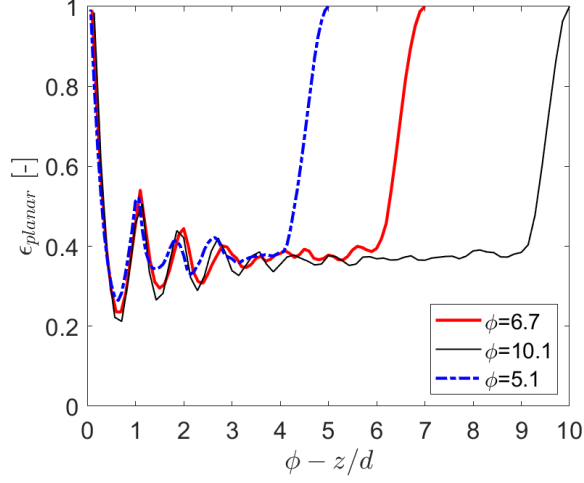
23

Figure 4: Flow-normal planar porosity ϵ_{planar} as a function of particle diameters d from porous medium base for $\phi = 6.7, 10.1, 5.1$.

surface is reached and the porosity decreases rapidly. It is clear from Figure 4 the change in porosity is heavily correlated to the position relative to the particle packing itself. We also observe that the maximum saturation values showed in Figure 3 are connected with the change in porosity. In fact, these values are $\max(Sat) \approx 0.8, 0.85, 0.9$ for $\phi = 5.1, 6.7, 10.1$ which implies that the infiltration rate is dramatically reduced when the liquid front approaches the bottom at a distance of approximately one particle diameter; this occurs right before the last particle layer. By looking at Figure 4 we notice that in the interval over the last particle layer the value of porosity exhibits a sudden increase. This observation suggests that pore throat expansions can act to impair liquid infiltration. In Subsection 3.3 we will confirm that this anomalous behaviour is induced by the rapid change of the morphology of the microstructure. More detailed quantification of the porous microstructure as a function of position in the medium requires a characterization of individual

24

⁴²⁷ pores themselves.

⁴²⁸ *3.2. Pore size distribution and infiltration depth*

⁴²⁹   In order to better characterize the porosity, individual pore size distri-
⁴³⁰ butions have been calculated and the mean and standard errors at each
⁴³¹ depth within the medium calculated. Note that while the geometries are 3-
⁴³² dimensional it is difficult to accurately determine and characterize pore sizes
⁴³³ in 3 dimensions, though attempts have been made, such as by Suh et al. [15]
⁴³⁴ and Liu et al. [16]. We have opted for characterization by analyzing pore
⁴³⁵ sizes in the plane lying perpendicular to the primary flow direction. This is
⁴³⁶ accomplished by taking slices of the domain at specific depths and utilizing
⁴³⁷ image analysis to extract equivalent diameters of the pores. The equivalent
⁴³⁸ diameter command returns the diameter d_{pore} of a circle with the equivalent
⁴³⁹ area as the imaged pore A_{pore}, using the equation

$$d_{pore} = \sqrt{\frac{4A_{pore}}{\pi}}. \tag{21}$$

⁴⁴⁰ The mean pore diameter and standard error are plotted in Figure 5 as a
⁴⁴¹ function of distance from the porous medium base, measured in particle
⁴⁴² diameters, exactly as in Figure 4. The standard error is computed as

$$s_{\overline{x}} = \frac{s}{\sqrt{n}}, \tag{22}$$

⁴⁴³ where s is the sample standard deviation and n is the sample size.

⁴⁴⁴   There is a noticeable jump in the mean pore size for $\phi = 10.1$ at a single
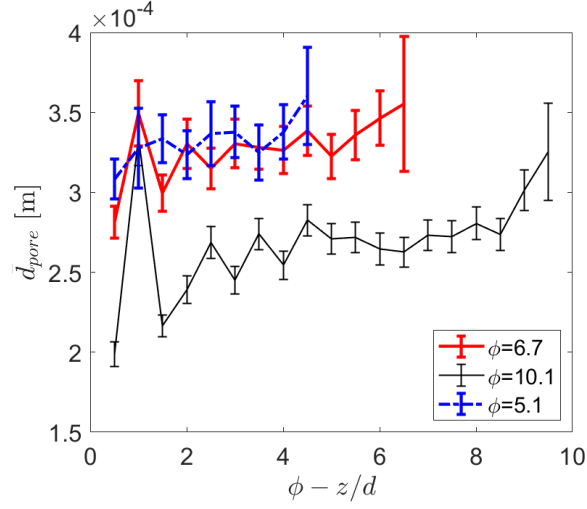⁴⁴⁵ particle depth from the bottom of the domain due to the packing. The jump

Figure 5: Pore diameter d_{pore} mean with standard error as a function of particle diameters d from porous medium base for $\phi = 6.7, 10.1, 5.1$.

is slightly less pronounced for $\phi = 6.7$ however there is little to no jump when $\phi = 5.1$. It should be noted that the values taken from the base of the medium are not shown as the mean pore sizes tend to infinity as porosity becomes 1. This reaffirms the oscillation of planar porosity seen in Figure 4. If one looks at the standard errors for each particle sized there is a trend from less variation in the smallest particle size to higher variation for the largest particle size, meaning the distribution of pore sizes is wider for the larger particles. The standard errors averaged over the depth of the medium are $\overline{s_{\overline{x}}} = 0.2, 0.14, 0.26$ for $\phi = 6.7, 10.1, 5.1$ respectively. This confirms the findings from the planar porosity analysis that the larger particle size and the uniformity of packing near the surface is relevant at the individual pore level. While the total porosity changes are similar, though not identical, the individual pore size changes are not as uniform in terms of magnitude.

As a consequence of higher variability in pore size distribution we expect

to see a less homogeneous flow pattern for a low value of the packing parameter ϕ, i.e. when the size of the medium depth is comparable with the particle size. In Figure 6 the normalized infiltration depths are plotted for the smallest particle size $\phi = 10.1$ in (a) and the largest particle size $\phi = 5.1$ in (b) at the same dimensionless time $t^* = 275$. This time was chosen as it clearly illustrates the difference in infiltration homogeneity between the different particle sizes. The penetration depth is determined by determining the deepest liquid node at each value in the flow-perpendicular plane.
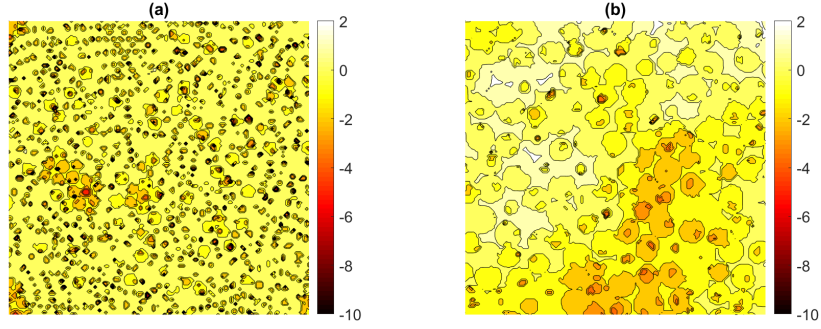
Figure 6: (a) Normalized distribution of liquid infiltration at $t^* = 275$ for $\phi = 10.1$. (b) Normalized distribution of liquid infiltration at $t^* = 275$ for $\phi = 5.1$. The color indicates standard deviations from the mean. Bo = 3.96.

By examining the normalized penetration depths for Figure 6 (a) and (b) we can see a marked difference in homogeneity of the flow. This agrees with the supposition that a wider variability of pore sizes in a thin medium can be linked directly to flow pathing preference, or ganglia formation. Ganglia here refers to finger-like structures comprised solely of liquid that penetrate farther into the microstructure than the bulk flow. In other words, it indicates an heterogeneous liquid front. Another quantification of the homogeneity of the water infiltration is given in Figure 7 where the probability distribution

27

functions (PDFs) for the infiltration depth are plotted. The timestep $t^* = 240$ is used when $\text{Bo} = 8.92$ due to the liquid reaching the base of the domain at higher time values for $\phi = 10.1$.
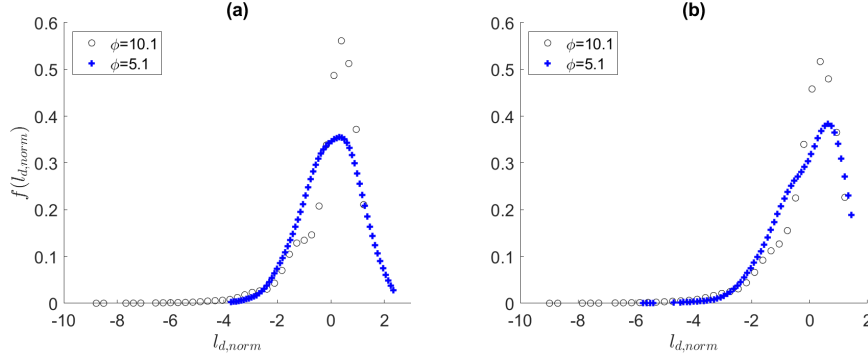

Figure 7: (a) PDF $f(l_{p,norm})$ of normalized liquid infiltration $l_{p,norm}$ at $t^* = 275$ for $\phi = 10.1, 5.1$ and Bo = 3.96. (b) PDF $f(l_{p,norm})$ of normalized liquid infiltration $l_{p,norm}$ at $t^* = 240$ for $\phi = 10.1, 5.1$ and Bo = 8.92. The x-axis indicates standard deviations from the mean.

The curves in both Figure 7 (a) and (b) indicate a larger distribution when $\phi = 5.1$ as seen from Figure 6 whereas the flow is highly homogeneous when $\phi = 10.1$ as seen by the high peaks at the mean value. A final point to be made is that the value of the Bond number does not radically change the infiltration pattern, thus enforcing the notion that the behaviour is not dependent primarily on the hydraulic head. With regard to the relationship between pore sizes and infiltration homogeneity it is highly likely the pore sizes themselves have a high impact on the infiltration dynamics. This is due to the energy required to fill the pores. This phenomena can be investigated by analyzing the liquid-gas interfacial area for each particle size.

3.3. Influence of liquid-gas interfacial area

Figure 8 gives the dimensionless liquid-gas interfacial area for each geometry as a function of dimensionless time. The clearest visible trends within the figures are the general slopes for all cases. When $\phi = 10.1$ and $\phi = 6.7$ we see a decrease over time in interfacial area for both hydraulic heads. The slope of the $\phi = 5.1$ case seems instead to oscillate around a constant value. The overall oscillation in interfacial area is indicative of liquid buildup at pore throat and subsequent sporadic jumping patterns of pore saturation. The $\phi = 5.1$ case displays small fluctuation amplitudes, suggesting slower infiltration in time.
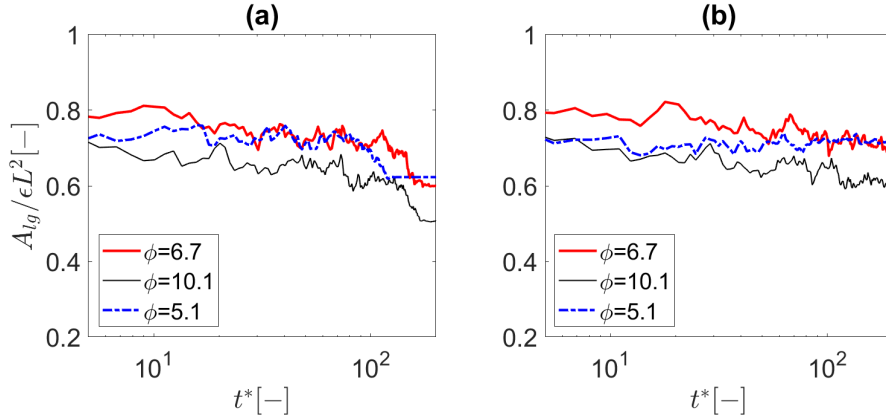

Figure 8: (a) Dimensionless liquid-gas interfacial area $A_{lg}/\epsilon L^2$ as a function of dimensionless time t^* for $\phi = 6.7, 10.1, 5.1$ with Bo = 8.92. (b) Dimensionless liquid-gas interfacial area $A_{lg}/\epsilon L^2$ as a function of dimensionless time t^* for $\phi = 6.7, 10.1, 5.1$ with Bo = 3.96.

The underlying cause of the intermittent behaviour of liquid-gas area buildup and possible stagnation lies in the balance of forces acting in the capillary structure and has been mathematically described firstly by Cassie and Baxter [18] for describing the mechanical balance rensposible for the behaviour of droplets leaning on rough surfaces. The same concept has been

29

applied for describing the rapid pore-scale displacement known as Haines
jump [41]. We can formalize such a force balance by applying the principle
of Helmholtz free energy F which describes the thermodynamic balance of a
isochoric and isothermal system as in (23).

$$
\begin{aligned}
dF &= \delta W < 0 && (23) \\
&= -\sum_{i=l,g} p_i dV_i + \gamma dA_{lg} && (24) \\
&= -(p_l - p_g)dV_l + \gamma dA_{lg} && (25) \\
&= -p_c d(Sat\ V_f) + \gamma dA_{lg} && (26) \\
dF^* &= -\frac{p_c V_f}{\gamma} + \frac{dA_{lg}}{dSat} < 0 && (27) \\
V_f &= \epsilon V_{tot} && (28)
\end{aligned}
$$

where p_l, p_g, p_c are the liquid, gas and capillary pressure, respectively; V_l, V_f, V_{tot}
are the liquid, total void, and total volume; and A_{lg} is the liquid-gas inter-
facial area. Applying the concepts of thermodynamics of surface tension
we rewrite Eq. (23) as Eq. (24). This equation represents the maximum
amount of reversible work done by such a system, and with a few algebraic
manipulations the resulting relation is given in Eq. (27).

This equation clearly shows the relationship between the interfacial area
derivative and capillary pressure. This relationship determines the energy
balance of the system: in presence of an interfacial area expansion, the cap-
illary pressure term must compensate to facilitate liquid infiltration. This
energy requirement can explain why drastic expansions, as the one induced
by the packed microstructure at the bottom of the medium, can considerably

30

reduce infiltration rate and possibly impede it. The continuous liquid buildup at the pore throat and rapid pore invasion mechanisms induced by packed microstructures give rise to intermittent infiltration behaviour at pore-level and anomalous reduced infiltration rate at the macroscopic scale.

Thus to further evaluate this formalized requirement we plot in Figure 9 the interfacial area as a function of saturation for all cases. In Figure 9(a) and 9(b) where infiltration occurs the general slope is negative so that the inequality in Eq. (27) is easily satisfied and infiltration occurs uniformly. In Figure 9(c) it is clear that especially under lower hydraulic pressure the area does not significantly decrease with saturation, indicating that Eq. (27) is possibly not satisfied in some pores and total infiltration of the medium is slowed down. In addition, infiltration fails when the area-saturation derivative is not sufficiently steep after some small initial increase. When this derivative condition is reached infiltration occurs, however this condition must be maintained for increasing saturation for the process to continue. If the interfacial area increment is too large to be sustained by the capillary pressure, infiltration will stop causing the packed bed to act like a capillary barrier.

Ross (1990) discussed capillary barriers and determined criteria for their size and liquid deflection capacity in analytical terms [17] in context of their diversion capacity. Diversion capacity in this case refers to the amount of liquid that can be channeled in a lateral direction by the interaction between an upper and lower layer of different sized particles. It is important to note that while the effect has been noted and studied, the conditions for the phenomenon to affect the infiltration process from a morphological perspec-

31

tive have not been quantified, to the best knowledge of the authors. This phenomenon clearly plays a role in infiltration dynamics, even when contact angles are near neutral. The morphological impact on liquid infiltration is expected to increase when the contact angle is reduced; thus quantifying its influence is of importance for cases with variable saturation, as is the case with rainfall infiltration of soils. Additional work must be undertaken to more accurately capture the pore size and distributions since the current method only characterizes them in a planar manner. A direct comparison of capillary pressure and the interfacial area-saturation derivative would be appropriate to validate the applicability of the equation and could be a critical aid in deriving conditions for infiltration failure.

3.4. Design considerations

From a design perspective we show the results of the six cases in this study in terms of the infiltration rate in Figure 10 and offer some insight into how these results can be applied in practice. This rate is quantified by α which is the exponent of the power law given in (20), at intermediate times. α can be considered as a measure of the ability of the microstructure to detain the infiltrating rainfall, with higher values corresponding to more rapid infiltration and shorter detention time. Therefore it is recommended to consider the microstructure with regard to depth and particle size in the design of a green roof, particularly when including thin substrate layers, when the thickness of the medium and the particle size are of the same magnitude. As we have seen in this study, larger particle sizes in relation to the porous media thickness may reduce infiltration as opposed to a substrate

32

consisting of smaller particles; this phenomenon being exacerbated by lower rainfall intensities. In addition there is merit in considering the climatic conditions in the location of installation as by taking local rainfall quantities into account in the design, it is possible to optimize the roof performance for extreme conditions where the benefit of a green roof is maximized. It is also possible to layer different particle thicknesses so as to create a substrate that is designed to perform optimally under variable conditions. By layering substrates in this way one can achieve the desired detention of rainfall in the green roof. This may be the most important takeaway from this study in regards to designing green roofs for variable climatic conditions in the most efficient way.

If one considers how these results can be combined with previous research into green roof performance there are a few points to consider. Firstly, we stress here that we have considered only the growth substrate and no vegetation is included. Blue roofs do not include vegetation and are primarily used for storm water management thus our results are directly applicable to such constructions. If vegetation is included we must consider the mechanical blocking effect at the surface however this simply reduces the quantity of surface water for infiltration. In addition, root networks will disturb the soil matrix and contribute to small channels throughout the medium where liquid can flow more easily. These channels may contribute to areas in the substrate where liquid will not reach as frequently and will be more hydrophobic. From a larger time scale the impact of evapotranspiration must be considered, however this process primarily affects the detention capacity of a green roof as it removes trapped water from the smallest pores rather

33

than the liquid able to infiltrate and drain out of the soil. Most green roof constructions also include a drainage layer directly beneath the root barrier layer and growth substrate layer. This means that at the base of the growth substrate the packing will resemble the physics where wall impacts will be significant. By applying the results presented here one can design the lowest particle layers in contact with the root barrier (wall) to facilitate the transfer of water from the growth substrate to the drainage layer. By combining the purely mechanical processes such as those studied in this work with the contribution from evapotranspiration we can generate a more accurate picture for designers that captures many factors critical to the performance of green roofs over singular rainfall events and over the longer term.
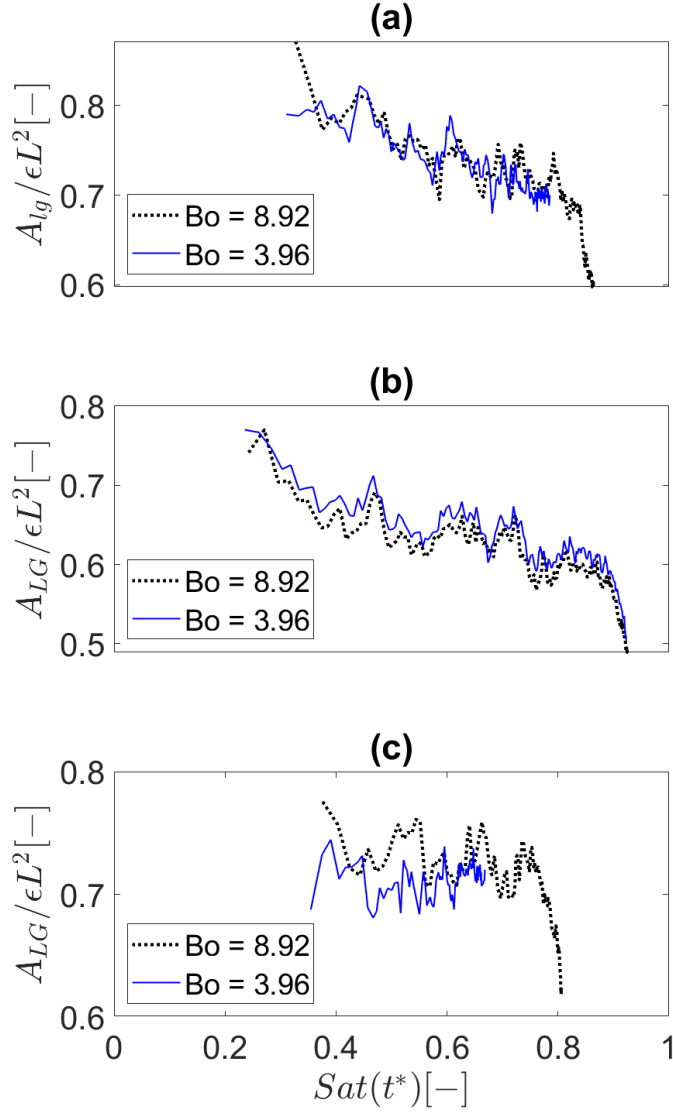
Figure 9: Dimensionless liquid-gas interfacial area $A_{lg}/\epsilon L^2$ as a function of saturation $Sat(t^*)$ for $\phi = 6.7$ (a), $\phi = 10.1$ (b), and $\phi = 5.1$ (c).
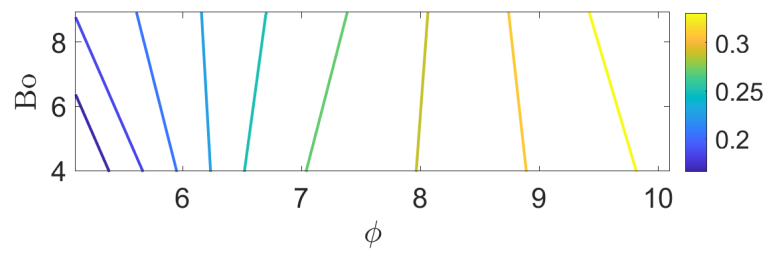
Figure 10: α extracted at intermediate times from Figure 3 plotted as a function of ϕ and Bo.

36

4. Conclusion

In this paper we have explored the effect of the microstructure on liquid infiltration into thin unsaturated porous media. Three microstructures defined by a unique packing parameter ϕ have been evaluated and infiltration is driven by 2 Bond numbers, representing different standing water heights on the porous medium surface. We have demonstrated the relationship between the microstructure and the flow homogeneity by analyzing saturation, liquid-gas interfacial area, pore size distribution, porosity, and infiltration depth. It is shown that the liquid-gas interfacial area plays a significant role in infiltration and is determined by the microstructure thickness in relation to the particle sizes. The analysis showed that while the total planar porosity of each domain remained similar, the effect of particle size in the homogeneity of the layering impacted the infiltration. This is due to the larger variation of pore sizes found in the domains with larger particles sizes, leading to increased inhomogeneous flow patterns. This result is formalized by applying the concept of Helmholtz free energy to liquid infiltration of a porous medium as the energy balance between capillary pressure and liquid-gas interfacial area. This balance is instrumental in determining the flow pattern within the microstructure as is dependent upon the structure itself. This behavior can be controlled by layering different microstructures within green roof substrates to optimize their performance with regard to rainfall detention time.

5. Acknowledgements

References

[1] J. Olsson, P. Berg, A. Eronn, L. Simonsson, J. Södling, L. Wern, W. Yang, Extremregn i nuvarande och framtida klimat analyser av observationer och framtidsscenarier (January 2018).
URL https://www.smhi.se/publikationer/publikationer/extremregn-i-nuvarande-och-framtida-klimat-analyser-av-observationer-och-framtidsscenarier-1.129407

[2] D. Lunain, D. Ecotiere, B. Gauvreau, In-situ evaluation of the acoustic efficiency of a green wall in urban area, in: Proceedings of the INTER-NOISE 2016 - 45th International Congress and Exposition on Noise Control Engineering: Towards a Quieter Future, 2016, pp. 6592–6601.

[3] H. Imran, J. Kala, A. Ng, S. Muthukumaran, Effectiveness of green and cool roofs in mitigating urban heat island effects during a heatwave event in the city of melbourne in southeast australia, Journal of Cleaner Production 197 (2018) 393–405. doi:10.1016/j.jclepro.2018.06.179.

[4] B. Johannessen, T. Muthanna, B. Braskerud, Detention and retention behavior of four extensive green roofs in three nordic climate zones, Water 10 (6) (2018) 671.

[5] S. Cascone, J. Coma, A. Gagliano, G. Pérez, The evapotranspiration process in green roofs: A review, Building and Environment 147 (2019) 337–355. doi:10.1016/j.buildenv.2018.10.024.

[6] V. Hamouz, J. Lohne, J. Wood, T. Muthanna, Hydrological perfor-

39

653 mance of leca-based roofs in cold climates, Water 10 (3) (2018) 263.

654 doi:10.3390/w10030263.

655 [7] V. Stovin, G. Vesuviano, H. Kasmin, The hydrological performance of a

656 green roof test bed under uk climatic conditions, Journal of Hydrology

657 414-415 (2012) 148–161. doi:10.1016/j.jhydrol.2011.10.022.

658 [8] S. Kemp, P. Hadley, T. Blanuša, The influence of plant type on

659 green roof rainfall retention, Urban Ecosystems 22 (2) (2019) 355–366.

660 doi:10.1007/s11252-018-0822-2.

661 [9] V. Stovin, S. Poë, S. De-Ville, C. Berretta, The influence

662 of substrate and vegetation configuration on green roof hydro-

663 logical performance, Ecological Engineering 85 (2015) 159–172.

664 doi:10.1016/j.ecoleng.2015.09.076.

665 [10] K. X. Soulis, J. D. Valiantzas, N. Ntoulas, G. Kargas, P. A. Nektar-

666 ios, Simulation of green roof runoff under different substrate depths

667 and vegetation covers by coupling a simple conceptual and a physi-

668 cally based hydrological model, Journal of Environmental Management-

669 doi:10.1016/j.jenvman.2017.06.012.

670 [11] A. Palla, I. Gnecco, L. Lanza, Unsaturated 2D modelling of

671 subsurface water flow in the coarse-grained porous matrix of

672 a green roof, Journal of Hydrology 379 (1-2) (2009) 193–204.

673 doi:10.1016/J.JHYDROL.2009.10.008.

674 [12] S. Schlüter, S. Berg, M. Rücker, R. Armstrong, H.-J. Vogel, R. Hilfer,

675 D. Wildenschild, Pore-scale displacement mechanisms as a source of

hysteresis for two-phase flow in porous media, Water Resources Research 52 (3) (2016) 2194–2205. doi:10.1002/2015WR018254.

[13] M. Porter, M. Schaap, D. Wildenschild, Lattice-boltzmann simulations of the capillary pressure-saturation-interfacial area relationship for porous media, Advances in Water Resources 32 (11) (2009) 1632–1640. doi:10.1016/j.advwatres.2009.08.009.

[14] Z. Li, S. Galindo-Torres, G. Yan, A. Scheuermann, L. Li, A lattice boltzmann investigation of steady-state fluid distribution, capillary pressure and relative permeability of a porous medium: Effects of fluid and geometrical properties, Advances in Water Resources 116 (2018) 153–166. doi:10.1016/j.advwatres.2018.04.009.

[15] H. S. Suh, D. H. Kang, J. Jang, K. Y. Kim, T. S. Yun, Capillary pressure at irregularly shaped pore throats: Implications for water retention characteristics, Advances in Water Resources 110 (2017) 51–58. doi:10.1016/J.ADVWATRES.2017.09.025.

[16] Z. Liu, A. Herring, C. Arns, S. Berg, R. Armstrong, Pore-scale characterization of two-phase flow using integral geometry, Transport in Porous Media 118 (1) (2017) 99–117. doi:10.1007/s11242-017-0849-5.

[17] B. Ross, The diversion capacity of capillary barriers, Water Resources Research 26 (10) (1990) 2625–2629. doi:10.1029/WR026i010p02625.

[18] A. B. D. Cassie, S. Baxter, Wettability of porous surfaces, Trans. Faraday Soc. 40 (1944) 546–551. doi:10.1039/TF9444000546.

41

[19] S. Succi, The lattice Boltzmann equation: for fluid dynamics and beyond, Oxford university press, 2001.

[20] D. Maggiolo, M. Seemann, H. Thunman, O. Santos, A. Larsson, S. Sasic, H. Ström, Self-cleaning surfaces for heat recovery during industrial hydrocarbon-rich gas cooling: An experimental and numerical study, AIChE Journal 65 (1) (2019) 317–325.

[21] Z. Guo, C. Zheng, B. Shi, Discrete lattice effects on the forcing term in the lattice boltzmann method, Phys. Rev. E 65. doi:10.1103/PhysRevE.65.046308.

[22] X. Shan, H. Chen, Lattice boltzmann model for simulating flows with multiple phases and components, Phys. Rev. E 47 (1993) 1815–1819. doi:10.1103/PhysRevE.47.1815.

[23] L. Chen, Q. Kang, Y. Mu, Y.-L. He, W.-Q. Tao, A critical review of the pseudopotential multiphase lattice boltzmann model: Methods and applications, International Journal of Heat and Mass Transfer 76 (2014) 210–236. doi:10.1016/j.ijheatmasstransfer.2014.04.032.

[24] H. Huang, M. Krafczyk, X. Lu, Forcing term in single-phase and shan-chen-type multiphase lattice boltzmann models, Physical Review E - Statistical, Nonlinear, and Soft Matter Physics 84 (4). doi:10.1103/PhysRevE.84.046710.

[25] A. De Maio, S. Palpacelli, S. Succi, A new boundary condition for three-dimensional lattice boltzmann simulations of capillary filling in rough

42

⁷²⁰ micro-channels, Communications in Computational Physics 9 (5) (2011)

⁷²¹ 1284—-1292. doi:10.4208/cicp.141009.241110s.

⁷²² [26] R. Benzi, L. Biferale, M. Sbragaglia, S. Succi, F. Toschi, Mesoscopic

⁷²³ modeling of a two-phase flow in the presence of boundaries: The con-

⁷²⁴ tact angle, Physical Review E - Statistical, Nonlinear, and Soft Matter

⁷²⁵ Physics 74 (2). doi:10.1103/PhysRevE.74.021509.

⁷²⁶ [27] J. Yang, E. Boek, A comparison study of multi-component lat-

⁷²⁷ tice boltzmann models for flow in porous media applications, Com-

⁷²⁸ puters and Mathematics with Applications 65 (6) (2013) 882–890.

⁷²⁹ doi:10.1016/j.camwa.2012.11.022.

⁷³⁰ [28] J. Reza, H. Martin, Analytical and numerical studies of separated lam-

⁷³¹ inar two-phase flow in elliptical ducts of arbitrary axis ratio, Chemical

⁷³² Engineering and Processing 24 (3) (1988) 121–132. doi:10.1016/0255-

⁷³³ 2701(88)80016-3.

⁷³⁴ [29] D. Bajare, A. Korjakins, J. Kazjonovs, I. Rozenstrauha, Pore struc-

⁷³⁵ ture of lightweight clay aggregate incorporate with non-metallic

⁷³⁶ products coming from aluminium scrap recycling industry, Jour-

⁷³⁷ nal of the European Ceramic Society 32 (1) (2012) 141–148.

⁷³⁸ doi:10.1016/j.jeurceramsoc.2011.07.039.

⁷³⁹ [30] P. Glover, I. Zadjali, K. Frew, Permeability prediction from MICP

⁷⁴⁰ and NMR data using an electrokinetic approach, Geophysics 71 (4).

⁷⁴¹ doi:10.1190/1.2216930.

[31] P. Glover, E. Walker, Grain-size to effective pore-size transformation derived from electrokinetic theory, Geophysics 74 (1). doi:10.1190/1.3033217.

[32] S. Galindo-Torres, A. Scheuermann, L. Li, Boundary effects on the Soil Water Characteristic Curves obtained from lattice Boltzmann simulations, Computers and Geotechnics 71 (2016) 136–146. doi:10.1016/j.compgeo.2015.09.008.

[33] G. Boccardo, F. Augier, Y. Haroun, D. Ferré, D. Marchisio, Validation of a novel open-source work-flow for the simulation of packed-bed reactors, Chemical Engineering Journal 279 (2015) 809–820–820. doi:10.1016/j.cej.2015.05.032.

[34] L. Slobozhanin, J. Alexander, S. Collicott, S. Gonzalez, Capillary pressure of a liquid in a layer of close-packed uniform spheres, Physics of Fluids 18 (8). doi:10.1063/1.2236123.

[35] J. C. Ramírez-Flores, J. Bachmann, A. Marmur, Direct determination of contact angles of model soils in comparison with wettability characterization by capillary rise, Journal of Hydrology 382 (1) (2010) 10–19. doi:https://doi.org/10.1016/j.jhydrol.2009.12.014.

[36] M. E. Schrader, S. Yariv, Wettability of clay minerals, Journal of Colloid and Interface Science 136 (1) (1990) 85–94. doi:https://doi.org/10.1016/0021-9797(90)90080-8.

[37] M. Fér, M. Leue, R. Kodešová, H. Gerke, R. Ellerbrock, Droplet infiltration dynamics and soil wettability related to soil organic matter of soil

44

aggregate coatings and interiors, Journal of Hydrology and Hydrome-chanics 64 (2) (2016) 111–120. doi:10.1515/johh-2016-0021.

[38] P. Raiskinmäki, A. Shakib-Manesh, A. Jäsberg, A. Koponen, J. Merikoski, J. Timonen, Lattice-boltzmann simulation of capillary rise dynamics, Journal of Statistical Physics 107 (1) (2002) 143–158. doi:10.1023/A:1014506503793.

[39] E. W. Washburn, The dynamics of capillary flow, Phys. Rev. 17 (1921) 273–283. doi:10.1103/PhysRev.17.273.

[40] C. A. Reynolds, H. Menke, M. Andrew, M. J. Blunt, S. Krevor, Dynamic fluid connectivity during steady-state multiphase flow in a sandstone, Proceedings of the National Academy of Sciences 114 (31) (2017) 8187–8192.

[41] W. B. Haines, Studies in the physical properties of soil. v. the hysteresis effect in capillary properties, and the modes of moisture distribution associated therewith, The Journal of Agricultural Science 20 (1) (1930) 97–116. doi:10.1017/S002185960008864X.